doi:10.26443/seismica.v5i2.2693

SEISMICA

Influence of Moho topography on seismic beamforming: implications for mantle scattering

Shubham Agrawal * [1], **Dan Frost** [1], **Philip Crotwell** [1]

[1]School of the Earth, Ocean, and Environment, University of South Carolina, Columbia, USA

Author contributions: *Conceptualization*: SA, DF. *Methodology*: SA, DF, PC. *Formal Analysis*: SA, DF. *Writing - Original draft*: SA, DF. *Writing - Review & Editing*: SA, DF, PC. *Supervision*: DF, PC. *Funding acquisition*: DF.

Abstract Measurements of scattered seismic phases are used to infer the distribution of small-scale heterogeneities in the mantle, which in turn inform our understanding of mantle dynamics. Directionality of the wavefront can be measured at seismic arrays, and accuracy is essential, as even small deviations can significantly misplace the inferred location of these scatterers. However, near-surface structures under seismic stations may distort these directionality measurements. In this study, we assess how variations in crustal thickness affect array measurements across Alaska. We observe backazimuth offsets mostly within 5° of the great-circle path between source and array, with offsets varying systematically between sub-arrays for each event, indicating a receiver-side origin. We test the hypothesis that offsets are caused by P-waves interacting with dipping Moho interfaces, and reproduce the observed offsets. We quantify how even modest tilts in the Moho (∼6°) can deflect the wavefront and alter apparent arrival direction by observable amounts. These offsets can shift inferred scatterer locations by hundreds of kilometers, illustrating the need to correct for shallow structure in deep Earth imaging studies.

Production Editor:
Andrea Llenos
Handling Editor:
György Hetényi
Copy & Layout Editor:
Miriam Gauntlett

Received:
2026-03-17
Accepted:
2026-06-26
Published:
2026-07-20

Non-technical summary Seismic waves recorded at the Earth's surface can reveal small-scale structures in the deep Earth by detecting how the waves scatter. The energy from the scattered waves is often small, but by combining data from multiple seismometers (called an array), we can detect and map the source of heterogeneity, known as scatterers. However, near-surface structures, particularly variations in crustal thickness, can distort the wavefronts before they reach the array. In this study, we show that these shallow structures can shift the apparent direction of incoming waves, potentially leading to large errors in locating scatterers. Correcting for these effects is essential for accurate imaging of the Earth's interior.

1 Introduction

Seismic station coverage across the globe has burgeoned significantly over the past decade, with regions of Earth bereft of seismic stations seeing new deployments. Large-scale seismic arrays, such as the US Transportable Array (IRIS Transportable Array, 2003), AlpArray (Hetényi et al., 2018), and the ongoing Western Australia Array (Murdie et al., 2024), have dramatically increased station density, enabling more detailed and widespread seismic investigations, particularly array based methods (e.g., Rost and Thomas, 2002, 2009). Array seismology utilizes recordings from multiple, often closely spaced, seismic stations to enhance signal detection and extract key seismic wavefield parameters. By coherently summing seismic signals through techniques like beamforming (e.g., Rost and Thomas, 2002), arrays significantly improve the signal-to-noise ratio, allowing the detection of low-amplitude arrivals that may be hard to unequivocally observe in single-station records. This enables the identification of scattered phases that deviate from the great-circle path, offering insights into lateral heterogeneities within the Earth's interior. For instance, array-based methods have been used to locate mid-mantle scatterers using P- and PP-waves (e.g., Rost et al., 2008; Bentham and Rost, 2014; Kaneshima, 2016; Schumacher and Thomas, 2016; Rochira et al., 2022; Yuan et al., 2023), map anisotropy in subduction zones (e.g., Wolf et al., 2022, 2024), detect mantle plumes (Gu et al., 2009; Stockmann et al., 2019; Rost et al., 2023), and image core-mantle boundary structures (e.g., Frost et al., 2013; Frost and Rost, 2014; Martin et al., 2023; Frost et al., 2024).

Earth's velocity structure, both closer to the source or receiver or along the raypath, can affect the propagation of a wavefront, leading to deviations from the theoretical travel path predicted for a 1D velocity structure. Such deviations in wavefront propagation manifest as discrepancies in measured slowness, which is the reciprocal of wave velocity projected onto the surface, indicating the apparent speed and angle of incidence of wavefront; and backazimuth, which is the direction from which the wave arrives, measured clockwise from north. It is well established that near-surface structure beneath the receiver is likely to have the most significant impact on wave direction, and several studies have developed empirical corrections for specific International Monitoring System (IMS) arrays, includ-

*Corresponding author: sagrawal@mailbox.sc.edu

ing: Warramunga, Australia (Wright et al., 1974); Gauribidanur, India (Ram and Yadav, 1984); Eilson, Alaska (Lindquist et al., 2007); Gräfenberg, Germany (Faber et al., 1986; Krüger and Weber, 1992); GERESS, Germany (Bokelmann, 1995a); Chiang Mai, Thailand (Tibuleac and Stroujkova, 2009); GSETT-3 alpha network (Koch and Kradolfer, 1997, 1999); LZDM, China (Hao and Zheng, 2010); Tripoli, Greece (Pirli et al., 2018); and a global compilation of IMS arrays (Bondár et al., 1999).

Wavefront deviations result from vertical and lateral variations in seismic velocity. For instance, mantle plumes can warp wavefronts due to thermal and compositional heterogeneity (e.g., Stockmann et al., 2019), while dipping features like subducting slabs can distort, deflect, and attenuate the wavefront, as noted in observations (e.g., Silver and Chan, 1986; Cormier, 1989) and numerical simulations (e.g., Vidale, 1987; Chen et al., 2007; Zhan et al., 2014; Pisconti et al., 2025). Such distortions are not limited to mantle studies; as shown by Frost et al. (2020), subducting slabs can even influence seismic energy that travels through the core, altering the interpretation of core-sensitive phases. Similarly, the topography of the Mohorovičić discontinuity (Moho) — a major seismic velocity contrast between the crust and mantle — can significantly influence seismic wave propagation, often producing larger deflections in backazimuth and slowness than those caused by more modest velocity anomalies, such as a 5% perturbation from a plume or slab (e.g., Niazi, 1966; Zengeni, 1970; Wright et al., 1974; Havskov and Kanasewich, 1978; Ram and Yadav, 1984; Hao and Zheng, 2010; Flanagan et al., 2012; Jacobeit et al., 2013; Colavitti et al., 2022; Li et al., 2024). Niazi (1966) provided a foundational theoretical framework, demonstrating that a dipping Moho causes seismic waves to deviate from their expected paths, resulting in azimuth-dependent variations in apparent backazimuth and slowness.

If unaccounted for, these effects can bias interpretations of subsurface structure. Subsequent studies have reinforced and extended these findings. For instance, Havskov and Kanasewich (1978) used array analysis to estimate the dip and strike of the Moho, showing that structural information could be extracted from systematic backazimuth deviations. However, these studies primarily utilized small- to medium-aperture arrays (tens of kilometers in scale), where aperture is defined as the maximum distance between two seismic stations within that array. It has been observed that backazimuth offsets originating from Moho tilt could be up to 20° (Hao and Zheng, 2010; Flanagan et al., 2012; Jacobeit et al., 2013; Li et al., 2024). Offsets in back-azimuth and slowness are of particular importance for scattering studies, where these parameters are used to ray-trace back from the array to the inferred location of the causative scatterer in the mantle. For a scattered P-to-P-wave at source receiver distance 80° and mid mantle scattering depths, which is typical for such studies, an offset in the observed scatterer backazimuth of 5° can shift the inferred scatterer location by up to 500 km. This illustrates how even moderate backazimuth anomalies can introduce large spatial errors in mantle imaging.

Traditionally, array seismology has been conducted using small-aperture arrays, typically with apertures less than 50 km, such as IMS arrays, except LASA and NORSAR. IMS arrays were often sited in areas with relatively simple subsurface geology (Bondár et al., 1999). IMS arrays have proven instrumental in detecting small-scale structures in the Earth (e.g., Frost et al., 2017, 2018). With the advent of denser and broader seismic deployments, it is now possible to construct sub-arrays with apertures of any size (e.g., Schumacher and Thomas, 2016; Rochira et al., 2022; Ward et al., 2023; Frost et al., 2024). While this increased scale enhances our ability to probe new regions and more complex structures, the lack of intentional control for subsurface structure and the possibility of larger aperture arrays exposes measurements to the influence of crustal heterogeneities, particularly the Moho discontinuity. In smaller-aperture arrays, seismic rays typically sample a relatively uniform portion of the crust, minimizing the impact of lateral structural variations. However, in large-aperture arrays, rays arriving at different stations may traverse significantly different paths, encountering variable Moho depths and gradients. These differences can distort the apparent slowness and backazimuth of incoming phases. Furthermore, arrays formed in different locations will experience different distortions, impacting inter-array comparisons. As large-aperture sub-arrays become more commonly employed in regional and global studies, it is essential to reassess how such structural variations can bias backazimuth and slowness, which are foundational to interpreting scattered wavefields. Although these effects have been considered for small, fixed-aperture arrays (e.g., Bondár et al., 1999), their influence on larger, flexible sub-arrays remains underexplored.

In this study, we use ray-theoretical modeling to simulate the effects of a tilted Moho on wavefront propagation and its impact on array-derived measurements (Section 2). We then focus on Alaska, a region of significant tectonic complexity and pronounced Moho topography, to quantify the extent of bias introduced by crustal structure (Section 3). We use P- and PP-waves (and their depth phases), which are commonly used to investigate mantle scatterers due to their strong amplitude and clarity across a wide range of distances (see Kaneshima, 2016, for a compilation of scattering studies). Finally, to establish the extent of this effect, we contrast Alaska with a tectonically less complex region (Section 3.6). Our goal is to develop a framework for recognizing and correcting these biases, thereby improving the reliability of array-based analyses in Alaska and other structurally complex regions.

2 Effect of tilt on seismic stations: tilted Moho case

A dipping subsurface interface, such as the Moho, can refract seismic waves off the great-circle path, resulting in observed backazimuth and slowness values at the receiver that differ from theoretical predictions from a 1D, plane-layered model (Niazi, 1966; Zengeni, 1970; Wright et al., 1974). We explore and quantify this effect using ray-theory models, both for a single seismic station (Section 2.1) and an array (Section 2.2). In this section, we use ray parameter and incidence angle to represent angle of the ray to the surface instead of slowness, as these quantities are directly related through the wave speed and are more intuitive for describing wavefront refraction at interfaces.

2.1 Application to single station

To understand the effect of the Moho tilt on the incoming raypath, we consider P- and PP-waves generated by a teleseismic earthquake intersecting the Moho surface from below. We consider a one layer crust over a mantle half-space, where x, y, and z are the two lateral and one vertical dimensions, respectively (Fig. 1). Z is positive upwards. The incident ray vector, $\hat{i}$, and the Moho normal vector, $\hat{n}$, are defined as:

$$\hat{i} = \frac{\mathbf{i}}{||\mathbf{i}||} \tag{1}$$

$$\hat{n} = \frac{\mathbf{n}}{||\mathbf{n}||} \tag{2}$$

These vectors are normalized to ensure that the resulting angles (e.g., angle of incidence) are independent of their magnitudes. The angle of incidence at the Moho, θ_i, is given by:

$$\cos\theta_i = \hat{i} \cdot \hat{n} \tag{3}$$

Applying Snell's law, the refracted ray vector, $\mathbf{r}$, can be expressed as:

$$\mathbf{r} = \frac{\mu_1}{\mu_2}\hat{\mathbf{i}} + \left(\cos\theta_r - \frac{\mu_1}{\mu_2}\cos\theta_i\right)\hat{\mathbf{n}} \tag{4}$$

where, μ_1 and μ_2 are the refractive index of mantle and crust, respectively, and θ_r is the angle of refraction.

We begin by assuming a P-wave velocity of 8 km/s in the mantle and 5.8 km/s in the crust, taken from the 1D velocity model iasp91 (Kennett and Engdahl, 1991). The Moho normal vector, $\mathbf{n}$, is defined as $[t, 0, 1]$, where t represents the horizontal tilt in the X-direction and 1 represents the vertical component. A value of $t = 0$ corresponds to a horizontally oriented Moho (no tilt), while increasing values of t indicate a greater tilt away from vertical in the X-direction. To quantify the impact of this tilt, we measure changes in the backazimuth and ray parameter of the refracted ray, $\mathbf{r}$, relative to the case of a planar (un-tilted) Moho (blue plane in Fig. 1a). Fig. 1b illustrates how a Moho tilted by 2.86° corresponding to a $\sim$25 km Moho depth change over 500km and representative of gradients observed in Alaskan Moho topography, (Section 3.5.1), alters the backazimuth of the refracted ray across a range of incidence angles at the Moho interface. We show results for three initial ray backazimuths: 0°, 45°, 90° (blue, green, and pink arrows in Fig. 1a). The incidence angle at the Moho varies depending on the wave type, with P-waves arriving at steeper angles than PP-waves for the same source-receiver geometry. This leads to differing sensitivities of the backazimuthal deviation to Moho tilt for the two phases.

When the ray path is aligned with the direction of the Moho tilt (backazimuth = 90°; pink dots in Fig. 1), there is no change in the backazimuth of the refracted ray. In contrast, when the incoming ray is orthogonal to the direction of tilt (azimuth = 0°; blue dots in Fig. 1), the backazimuth of the refracted ray deviates most significantly from its original value. Furthermore, the shift in backazimuth is greatest for steeply incident rays and decreases with increasing incidence angle. This implies that P-waves, which typically have steeper ray paths, are more refracted by the Moho tilt than PP-waves, which tend to have shallower incidence angles. Moreover, observations at greater source-receiver distances, from which rays arrive more steeply, will be more affected. In the intermediate case where the initial backazimuth is 45° (green dots in Fig. 1), the magnitude of the backazimuth shift falls between the two end-member scenarios described above.

To further investigate the effect of Moho tilt, we double the tilt angle to –5.7° ($\sim$50 km Moho depth change over 500km) and reverse the direction of tilt (Fig. 1c). We observe that the deviations in backazimuth are approximately doubled and occur in the opposite direction, consistent with the expectation that, for small tilt angles, angular deviations scale linearly with tilt. Similarly, Figs 1d,e illustrate changes in the ray parameter when a ray encounters a tilted Moho (same Moho configuration as in Figs 1b,c). In contrast to the trends observed for backazimuth deviations, the ray parameter at the surface varies across all three incoming ray azimuths. This occurs because the incidence angle relative to the Moho changes with the tilt, regardless of the backazimuth of the incoming ray. The largest deviation in the ray parameter is observed when the ray path aligns with the direction of the greatest Moho tilt: that is, a backazimuth of 90° (the same as the X-axis). Notably, the ray parameter is less sensitive to the incident angle of the incoming ray, exhibiting a much flatter trend compared to the trends in backazimuth (Fig. 1b).

From our initial ray analysis, we observe that: 1) A tilted Moho has the greatest impact on the backazimuth of a ray when the tilt is perpendicular to the ray path, while it has little to no effect on the ray parameter. 2) Conversely, when the Moho tilt is aligned with the ray path, the backazimuth remains unchanged, while the ray parameter is most affected. 3) Steeper ray paths are more susceptible to backazimuth deviations due to Moho tilt, whereas shallower paths experience greater deviations in ray parameter. 4) Larger Moho tilt magnitudes lead to increased deviations in both backazimuth and ray parameter of the refracted ray. These observations and trends are consistent with the values reported by Niazi (1966). For a Moho dip angle of 5° and a velocity contrast of 0.7, they estimated backazimuthal deviations of 7° to 4° for incident angles between 20° to 40° (Table 2B in Niazi, 1966). In Fig. 1c, for a comparable Moho dip ($\sim$5.7°) and velocity contrast (0.725), we observe deviations ranging from 6.5° to 4°, suggesting agreement between our measurements and their predictions. Further, these deviations become significant when they exceed the resolution of the beamforming, or when they are large enough to substantially misplace

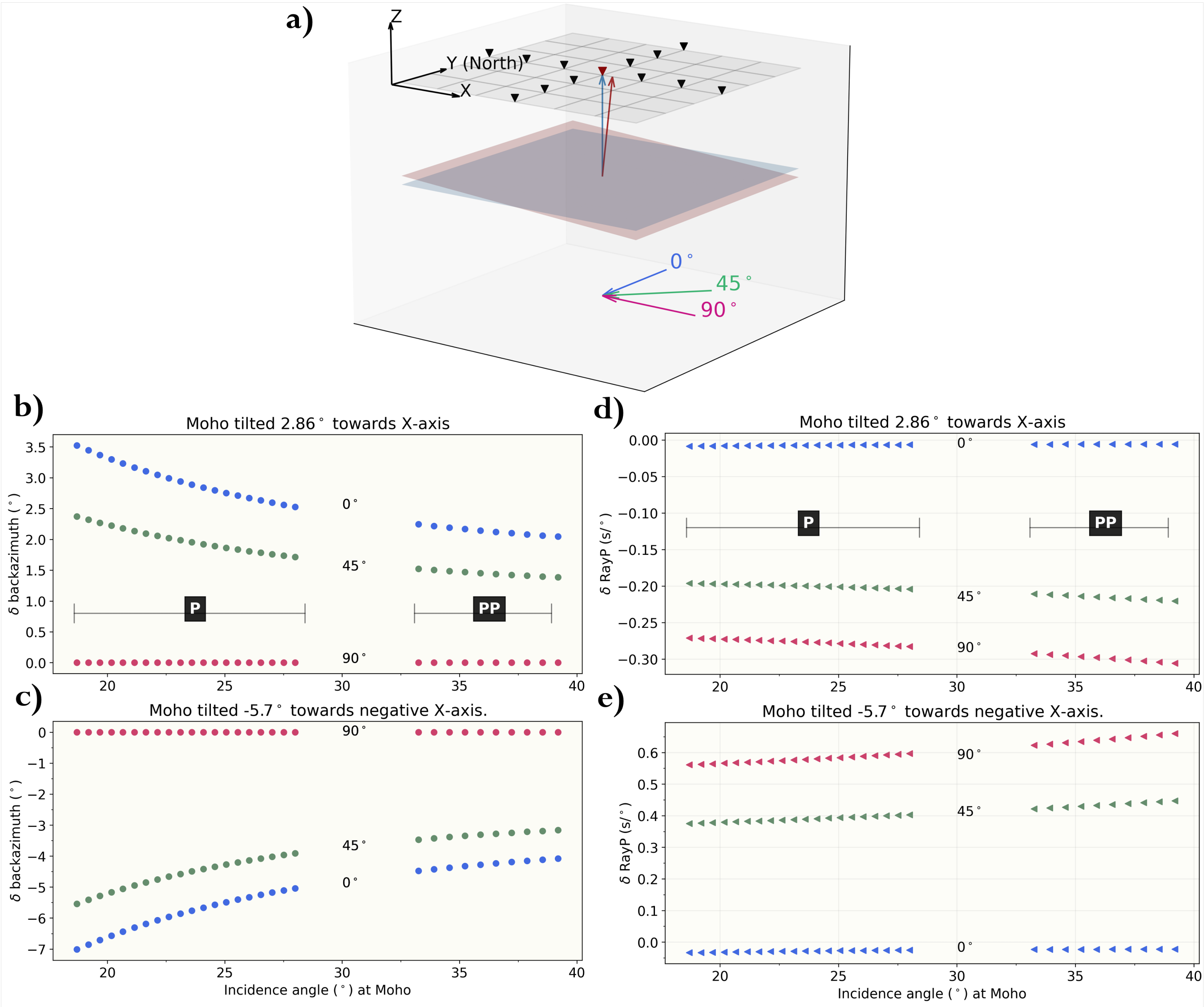

Figure 1 (a) Schematic of the setup for P- and PP-waves interacting with a Moho tilted by 2.86° towards the positive X-axis (red plane; red arrow is normal to this plane). The blue plane is horizontal. Backazimuth and ray parameter (horizontal slowness) are measured at the red station for the single-station case, while the black and red triangles indicate the array used in Section 2.2. Colored arrows show the three incoming ray backazimuths tested. (b) Backazimuth change, relative to planar Moho (blue plane in a), measured at the red station across a range of incidence angles for P- and PP-waves for the tilted Moho. (c) Same as b, but for a 5.7° Moho tilt away from the X-axis, opposite to the direction in a). (d,e) Same as (b,c), but for ray parameter.

inferred scatterer locations. As mentioned in Section 1, a backazimuth offset of 5° can shift a scatterer location by hundreds of kilometers. The phase-dependence of these offsets is also of relevance, as differential Moho-induced offsets between P- and PP-waves could be misinterpreted as evidence of off-path scattering if near-receiver crustal structure is not properly accounted for.

2.2 Application to an array of stations

Building on the principles established for a single station, we now investigate the effect of Moho tilt on a seismic array. We consider an array consisting of 13 stations (similar to the minimum number of stations used later for Alaska in Section 3), all located at the same elevation, in a cross shape with an aperture of approximately 5° (Fig. 2a), representative of the aperture we apply to Alaska later. We also performed the same experiment using a circular array of radius 2.5° and found that the results were equivalent to the cross case. To estimate the apparent direction and ray parameter of a seismic wavefront across an array, we calculate the relative arrival times of the wave at each station (e.g., Rost and Thomas, 2002). For a planar wavefront, the predicted arrival time at each station can be calculated based on its relative position with respect to the array centre and the direction of wave propagation, using the following expression from Schweitzer et al. (2012):

$$t_{\mathrm{n}} = \frac{-x_{\mathrm{n}} \cdot \sin\phi - y_{\mathrm{n}} \cdot \cos\phi}{V_{app}} \tag{5}$$

Here, t_n is the arrival time at station n, x_n and y_n are the station coordinates relative to the array center, ϕ is the backazimuth (measured clockwise from the positive y-axis in the x-y plane), and V_{app} is the apparent velocity beneath the array.

The apparent velocity at which the wavefront is observed to move across the array, V_{app}, is related to the P-wave velocity in the crust, V_{crust}, and the angle of incidence i (measured from the vertical z-axis), as:

$$V_{app} = \frac{V_{crust}}{\sin i} \tag{6}$$

To investigate the effect of a tilted Moho dipping at 5.7° in the x-direction (setup in Fig. 1a; Moho depths beneath each station shown in Fig. 2a), we begin by assuming a plane wave arriving with a range of backazimuths (0–90°), with the incidence angle fixed at 13.7° corresponding to the steepest angle of incidence for a direct P-wave at the largest possible source–receiver distance, i.e., before the P shadow zone. This configuration is chosen to accentuate the effect of Moho tilt on wavefront distortion. We measure time delays of this wave at each station in the array, using Equation 5. We trace rays through the mantle, Moho, and crust to each station and calculate the arrival time at each station. We then estimate the wavefront direction and incidence angle by minimizing the sum of squared residuals between observed arrival times and those predicted by a planar wavefront model, treating backazimuth and incidence angle as free parameters. The optimization is performed using the Nelder-Mead algorithm, initialized from a fixed starting point (5°, 5°), with the incidence angle constrained to physically reasonable values (0–90°). The resulting best-fitting parameters represent the apparent wavefront direction and incidence angle for the array, plotted as circles in Fig. 2b. We find that the array records a maximum backazimuth deviation of approximately 7° when the incoming ray's backazimuth is perpendicular to the Moho dip direction, which is consistent with the single-station case (Fig. 1b). A similar trend is observed in the ray parameter, suggesting that the effect of Moho tilt on apparent backazimuth and ray parameter is similar for an array and a single station.

Given the dip of the Moho, the crustal thickness beneath each station will differ. Stations located where the Moho tilt results in thinner crust (lighter blue shaded triangles) will record earlier arrivals, as seismic rays traverse a shorter crustal path (Fig. 2a). Here, we calculate the effect of this on the measured slowness and backazimuth. Assuming a total thickness h for the crust and mantle combined, z_{Moho} is the depth of the Moho beneath the station, d_z is the vertical component of the ray direction, $||d||$ is the total ray path length, and V_{crust}, V_{mantle} are the P-wave velocities in the crust and mantle, respectively, the total P-wave travel time at each station can be expressed as:

$$T_{\text{total}} = \frac{z_{\text{Moho}}}{d_z} \cdot \frac{\|\mathbf{d}\|}{V_{\text{crust}}} + \frac{(h - z_{\text{Moho}})}{d_z} \cdot \frac{\|\mathbf{d}\|}{V_{\text{mantle}}} \tag{7}$$

These crust-mantle travel-time estimates (with respect to the array centre and using V_{crust}, V_{mantle} as 5.8 km/s and 8 km/s, respectively) are used to perform the optimization for backazimuth and incidence angle, and the results are shown as plus symbols in Fig. 2b. The maximum backazimuth deviation is approximately 0.6°. We find that refraction at the tilted Moho in the X-direction shifts the wavefront toward the X-parallel direction, thereby altering arrival times. The crust–mantle travel-time correction produces a shift in the same sense, but with a much smaller magnitude. Consequently, less than 10% of the total backazimuth deviation associated with the tilted Moho can be attributed to the crust–mantle travel-time correction.

For a tilted Moho, the effect on the observed backazimuth and slowness measured by an array is analogous to the single-station case, an array exhibits the same qualitative behavior, and the four conclusions drawn in Section 2.1 remain valid when extended to arrays. The primary difference is that the maximum changes in backazimuth and ray parameter observed at the array level are slightly reduced relative to the single-station case, owing to the inclusion of crust–mantle travel-time corrections. In practice, however, real seismic arrays do not sample a Moho with uniform tilt beneath all stations. Nevertheless, this idealized framework provides a useful reference against which the observations from Alaska can be compared.

3 Effect of tilt on real data: Alaska

3.1 Data and pre-processing

To investigate the effect of Moho tilt on real data, we apply beamforming to measure slowness and backazimuth of P-waves measured at seismic arrays at stations in Alaska. Alaska serves as an ideal case study due to its complex Moho topography (Section 3.5.1) and extensive coverage with seismic stations. We selected global earthquakes between January 2020 and June 2024, at epicentral distances between 65° and 120° from the stations in Alaska, with magnitudes Mw $\geq$ 6.7 and source depths greater than 60 km to ensure simpler source time functions and clearer separation of the direct P arrival from its depth phases (e.g., Kaneshima and Helffrich, 2010; Bagley et al., 2013). In total, we analyzed 31 events (inset Fig. 3) recorded at 375 seismic stations, primarily distributed throughout Alaska, with some located in Canada.

For each event, we constructed sub-arrays from the available stations. To construct sub-arrays, we discretized the study region into a 2°×2° grid and searched for stations located within 2.5° of each grid point, allowing for overlap of stations between adjacent sub-arrays. A sub-array was formed at a given grid point if at least 14 stations were found within the defined radius, as fewer than that resulted in aliasing artifacts. On average, 28 sub-arrays were formed for each earthquake, with an average aperture of 507 km, with 90% of the apertures used between 400 and 550 km. An example sub-array is shown in Fig. 3 (magenta stations), with an aperture of 527 km. We did not enforce a specific array geometry in our analysis; the reader is referred to Frost et al. (2024) for a discussion on the sensitivity of beamforming results to the shape of the array.

For each event, vertical (Z) component seismic data were linearly detrended and demeaned, and the instru-

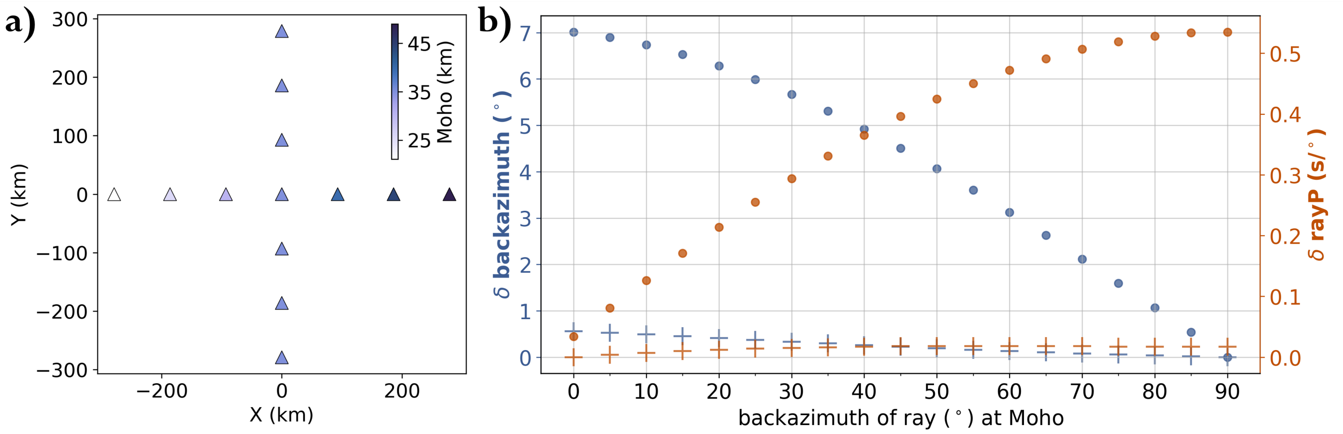

Figure 2 Effects of Moho tilt on seismic wave propagation beneath the array. (a) Moho depths beneath the array for a Moho tilted by 5.7° toward the X-axis. (b) Backazimuth and ray parameter changes measured at the array for a 5.7° Moho tilt toward the X-axis, calculated across a range of backazimuths using Equation 5 (shown as circles). Calculations including the effect of differential travel times through the crust and mantle due to Moho geometry (using Equation 7) are shown as plus symbols.

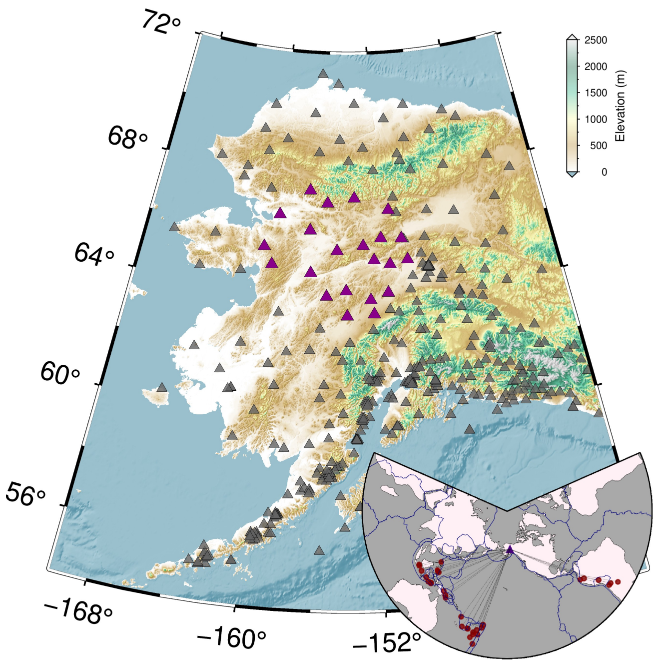

Figure 3 Seismic stations (grey triangles) and earthquakes (red circles in inset) used in this study. An example sub-array, magenta stations, has an aperture of 527 km and includes 22 seismic stations.

ment response was removed. The data were then band-pass filtered between 0.05–0.5 Hz, a frequency range found to be most effective for detecting P-waves relative to background noise during the beamforming procedure described in the following sub-section. Stations exhibiting spurious signals were excluded following visual inspection.

3.2 Beamforming methodology

We use beamforming to measure the slowness and backazimuth of coherent energy associated with teleseismic P, PP, and P-depth phase slownesses (P, P_{diff}, pP, sP, PP) (Davies et al., 1971; Rost and Thomas, 2002). Rather than analyzing individual phases separately, we use a single time window that encompasses all of these phases and includes all arrivals that fall within the expected time and slowness ranges. We construct beams by cutting the time series from 20 seconds before the expected arrival of the P (or P_{diff}) phase to 40 seconds after the PP phase, based on the iasp91 model (Kennett and Engdahl, 1991). We form beams to construct vespagrams by grid-searching for slownesses between 0 and 10 s/° in 0.25 s/° increments, and backazimuths between ±50° of the great-circle path in 1° increments. In order to reduce aliasing and enhance the precision of slowness and backazimuth determination, we compute a coherence metric called the F-statistic (Selby, 2008; Frost et al., 2013). The coherence, F, is calculated as the ratio of the total squared energy within the beam, $b(t)$, to the total squared differences between the beam and the individual traces $x_i(t)$ that are utilized to form the beam, within a time window M, normalized by the number of traces in the beam, N:

$$F = \frac{(N-1)}{N} \frac{\sum_{t=1}^{M} b(t)^2}{\sum_{i=1}^{N} \sum_{t=1}^{M} (x_i(t) - b(t))^2} \tag{8}$$

We compile these into F-trace vespagrams, which display coherence as a function of time, slowness, and backazimuth (with respect to the great-circle path). Further, prior to beamforming, we account for the individual topography beneath each seismic station by converting station elevation to a travel-time correction using a P-wave crustal velocity of 3 km/s and incorporating this correction into the moveout calculation.

3.3 Coherence and quality control

We apply the above process to all sub-arrays for all events, resulting in 778 vespagrams. We then analyze the vespagrams to determine their quality. A high-quality vespagram is characterized by compact regions (lobes) of high coherence around the phases of interest that are well-resolved in time, slowness, and backazimuth (Figs 4a,b). To differentiate between high-quality and noisy vespagrams, we compute the maximum coherence in the entire backazimuth vespagram and divide it by the mean coherence. If this Max/Mean ratio exceeds 20 (based on trial and error), meaning that there are clear peaks of coherence associated with well-resolved phases, the vespagram is retained for further analysis. This process removes 28% of the vespagrams. This threshold was introduced as an automated quality-control criterion for this dataset and may require retuning for different noise levels, station density, or array geometry.

To quantify measurement uncertainty, we select the top 5% of coherence values within a ± 5 s window around the absolute peak (marked by the maroon diamond in the backazimuth vespagrams—Figs 4b,d) in both slowness and backazimuth. The slowness and backazimuth ranges of this top 5%, shown as the width between the solid white bars in Fig. 4, provide uncertainty estimates and serve as an additional quality metric, whereby larger ranges indicate a more poorly resolved peak.

3.4 Constraining backazimuth offsets

For an example event (Fig. 4b), the energy of the seismic phases of interest arrives along the great-circle path, i.e., with a relative backazimuth of 0°. Meanwhile, vespagrams calculated for another event show deviations of the phases from the great-circle path (Fig. 4d). In this case, the energy is consistently offset from the great-circle path (dashed red line in Fig. 4d). A similar discrepancy was observed in the slowness, though the offsets were generally smaller in magnitude, close to or smaller than our resolution of 0.25 s/°. As demonstrated in Section 2.2, variations in backazimuth are more pronounced than those in slowness and exceed the resolution limits of our analysis. Therefore, our analysis focuses primarily on backazimuth offsets.

We identify arrivals in order to quantify their backazimuth offsets by calculating maximum coherence across all backazimuths within 5-second moving time windows with 50% overlap (colored circles in Figs 4e,f). Significant peaks were selected from this coherence timeseries using a prominence-based algorithm: we retained only peaks whose amplitude exceeded 25% of the global maximum and whose prominence, defined as the peak height relative to the surrounding local background, exceeded 10% of the global maximum (plus symbols in Figs 4e,f). These thresholds were chosen for this dataset so that only well-defined, physically meaningful peaks were used, suppressing noise and weaker incoherent or off-path energy. Significant peaks appear as darker lobes in Fig. 4d and corresponding peaks in Fig. 4f). In the example shown, these arrivals are consistently shifted toward more positive backazimuths. To account for slowness-dependent variability of back azimuth anomalies as noted in Section 2.2 and Fig. 2, we divide the vespagrams into two regions: low-slowness (P and P-depth phases) below 6 s/° (dashed black line), and high-slowness (PP and PP-depth phases) above 6 s/°. We then compute the mean backazimuth of significant peaks (plus symbols in Fig. 4f) in each region, yielding backazimuth offsets of 4° (low-slowness) and 3° (high-slowness) for the example shown, with larger offsets as expected for lower-slowness phases. Ward et al. (2021) developed an automated method to identify arrivals in slowness vespagrams with formal uncertainty estimates. While their approach is optimized for characterizing specific phases within a focused time window, our vespagrams encompass multiple phases simultaneously (up to ∼15 energy lobes in some cases), making a prominence-based peak-finding more appropriate.

3.5 Understanding backazimuth offsets in Alaska

For each sub-array and each event, we calculate the mean backazimuth offset (colored circles in Fig. 5a). We find that 95% of the mean offsets lie between -5° to 5° and individual sub-arrays often exhibit distinct mean offsets (discussed in the next paragraph). 14% of all measurements fall within $\pm 0.5°$ of the great-circle path, which we consider below our detection threshold and thus classify them with no significant offset (black circles in Fig. 5a). Importantly, measurements for nearly all earthquakes exhibit some degree of backazimuth offset, suggesting that these deviations are not specific to individual events.

We find that the sign and magnitude of backazimuth offsets depend on sub-array location (Fig. 5b). Furthermore, we find consistency of the offsets between earthquakes, but some sub-arrays do record conflicting offset directions. We further explore causes of these exceptions in Section 4.3. Nonetheless, the fact that the same earthquake yields varying offsets between sub-arrays suggests that the origin of these offsets is likely on the receiver side, as the raypath to different sub-arrays diverges beneath Alaska. In the following section, we compare the offset patterns with the results from Section 2.2, focusing on their relation to the Moho gradients beneath Alaska.

3.5.1 Impact of the Alaskan Moho

As demonstrated in Section 2.2, a sloped Moho surface can refract incoming seismic wavefronts, resulting in different slownesses and backazimuths than predicted. In this section, we evaluate whether the backazimuth offsets observed in Alaska are consistent with the region's crustal architecture. For this, we use a model of the Alaska Moho depths (Miller and Moresi, 2018, Fig. 5c) constructed using receiver functions. The depth of the Moho varies substantially across the region, from as shallow as ∼25–30 km beneath the forearc to ∼45–50 km beneath the Yukon-Tanana and Farewell terranes, resulting in numerous localized highs and lows, and consequently sharp Moho gradients.

Our sub-arrays have apertures of 300–550 km (Fig. 3), effectively averaging the Moho gradient over a large scale. Moreover, each ray samples the Moho only along its backazimuth, not necessarily the steepest gradient.

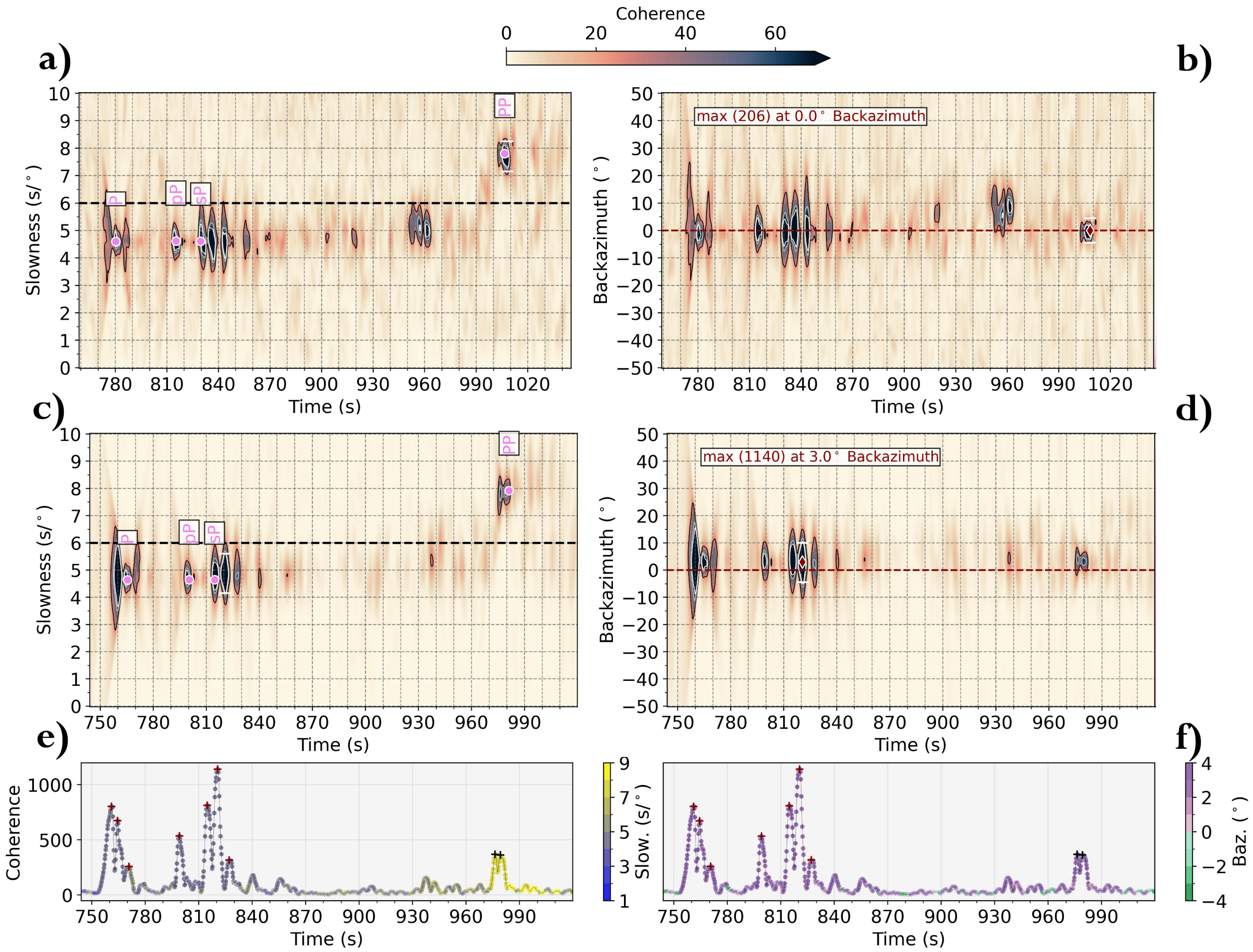

Figure 4 Vespagrams and measurement of backazimuth offsets. (a) An example of a well-constrained vespagram in slowness–time space with contours drawn as solid white lines. The black dashed line separates low- and high-slowness regions. Predicted arrival times and slownesses are shown as pink circles. (b) Same as (a), but in backazimuth–time space, measured relative to the great-circle path (red dashed line). The red diamond marks the point of global maximum coherence. (c,d) Same as (a,b), but for a different earthquake–sub-array pair exhibiting backazimuth offsets. (e,f) Peaks corresponding to high-coherence regions in slowness–time (e) and backazimuth–time (f) space for vespagrams in c and d. Circles are colored by the slowness or backazimuth value of the coherence maximum within a 5-second moving time window. Crosses indicate prominent peaks identified by the peak-picking algorithm. The mean backazimuth offset for prominent peaks in the low-slowness region (≤6 s/°) is 4°.

Therefore, we calculated directional Moho gradients using a 2.5° radius for azimuths in 10° increments. An example Moho gradient map calculated in the approximate backazimuthal direction of the majority of the observations (-130°) is shown in Fig. 5d. The Moho gradients in all directions range from -6.7 to 7.7 km/° (Fig. 6), which corresponds to equivalent tilts of up to 8° under the small-angle approximation, consistent with the range explored in our synthetic tilted-Moho models (Section 2.2). Our synthetic tests produce backazimuth offsets up to 7° (Fig. 2b), which are comparable to our measured backazimuths. Fig. 6 shows the observed backazimuth offsets with respect to the directional Moho gradient. We find that 62% of observations have consistent polarity between the directional Moho gradient and the backazimuth offset, indicating a modest but statistically significant relationship. A Spearman rank test yields ρ = 0.25, indicating a weak monotonic relationship between the two parameters. A randomization test (10,000 shuffles of the backazimuth offsets) confirms this is unlikely to arise by chance, with both the observed ρ (0.25) and sign-agreement value (62%) exceeding all 10,000 permuted values. However, there is considerable scatter in the data, which suggests that Moho topography is a primary but not exclusive control on the observed offsets, and we explore the potential causes of this in Section 4.3.

3.6 Control Case: Flat Moho region in US

To reinforce our interpretation that the backazimuth offsets observed in Alaska are indeed caused by crustal structure, we conducted a beamforming analysis using stations located in a region with relatively flat Moho topography. For this comparison, we selected Trans-

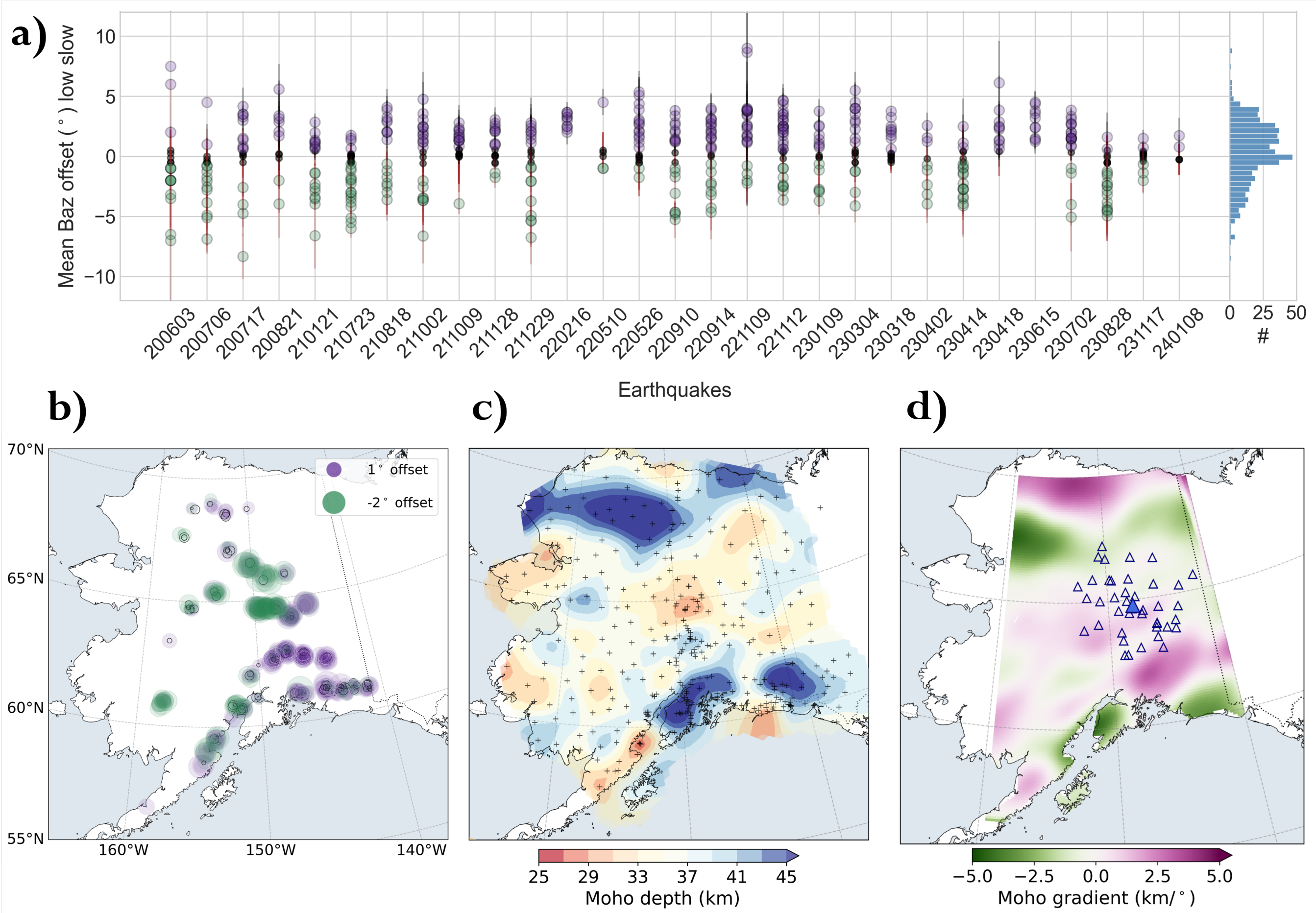

Figure 5 Distribution of backazimuth offsets for low-slowness phases (≤6 s/°). (a) Mean backazimuth offsets are shown as circles for each earthquake and each sub-array (positive: magenta; negative: green), with standard deviations indicated by vertical bars. Offsets within ±0.5°, considered below the detection threshold, are plotted as black circles. The histogram on the right highlights the significant number of non-zero backazimuth offsets. (b) The same backazimuth offsets are plotted at the center of their respective sub-arrays. Circle size reflects the magnitude of the offset. Due to lower station density in western and northern Alaska, most measurements are from central and southern Alaska. (c) Moho surface derived from receiver functions point measurements (black crosses) from Miller and Moresi (2018). (d) Directional Moho gradient calculated using a 2.5° radius spatial window in the -130° backazimuth direction, based on the Moho surface shown in (c). Blue triangles indicate the seismic stations forming an example sub-array, with the filled triangle marking the array center. The sub-array aperture and the spatial scale over which the Moho gradient is averaged are comparable.

portable Array (TA) stations deployed between 2012 and 2014 in the central United States, where the Moho is demonstrated to be more laterally uniform than Alaska (Fig. 7c; Shen and Ritzwoller, 2016), varying in depth between 40 and 48 km. Using the method described earlier, we constructed sub-arrays and calculated vespagrams for each earthquake. We found that 95% of the mean backazimuth offsets for these sub-arrays lie between -2.50° and 2.50°, with significantly reduced range from maximum to minimum compared to the Alaskan arrays (Figs 7a,b). Although minor offsets remain, their magnitudes are much smaller than those observed in Alaska. This serves as a control case to confirm that, in the absence of significant Moho gradients, such offsets are minimal or absent.

4 Correction and uncertainties

The contrast between the backazimuth deviations observed in Alaska versus those in the Central US suggests that complex Moho structure plays a key role in generating backazimuth deviations. This underscores the importance of accounting for local crustal effects when conducting beamforming studies in tectonically complex regions.

4.1 Correcting vespagrams for near-surface structure

To accurately locate scattering sources, it is essential to correct vespagrams for observed backazimuth offsets arising from near-surface structure, particularly Moho topography. As mentioned in Section 1, deviations on the scale observed in Alaska can lead to mislocations of scatterers by several hundred kilometers. Here, we have demonstrated that backazimuth offsets are most likely produced by refraction at a dipping Moho beneath the receivers. We therefore seek to estimate and correct these offsets before interpreting array-derived direction measurements.

Figure 6 Comparison of directional Moho gradients beneath each sub-array and the observed backazimuth offsets (color convention is the same as in Fig. 5a). The gradients are calculated using a spatial window of 2.5° radius in the direction of each earthquake backazimuth. The yellow diamonds correspond to the mean backazimuth offsets for the positive and negative offset populations.

To estimate the Moho geometry responsible for the observed backazimuth offsets from the great-circle path, we use the backazimuth and slowness measurements to reconstruct the wavefront geometry at the surface for all slowness and backazimuth pairs in a vespagram. Assuming that the entire offset arises due to refraction at the Moho, we back-project these rays to the base of the crust and apply Snell's Law to compute their incidence angles beneath the interface. In this back-projection, we use the same P-wave velocities adopted in Section 2.2, with V_{crust}, V_{mantle} as 5.8 km/s and 8 km/s, respectively. We then search for the direction and magnitude of Moho dip that would produce a wavefront deflection matching the observed offsets for the entire vespagram. We can then apply the shift associated with this tilt to the vespagrams, ideally realigning all measurements back to the great-circle path. An example outcome of this process is shown in Fig. 8, where the Moho dip required to reconcile the offset was 2.7°.

Because Moho gradients vary spatially across Alaska and vary locally with azimuth (Fig. 5d), a uniform correction across all events or sub-arrays would be inappropriate. Indeed, as demonstrated in Fig. 5a, different earthquakes exhibit different offset patterns, as do the same earthquake at different sub-arrays. To address this, we perform event and sub-array specific corrections based on the local Moho geometry. With this correction applied, the primary phases (P, pP, sP, PP) align with the theoretical great-circle path (Fig. 8b). Any remaining backazimuth deviations can then be attributed to scattering or other propagation effects along the raypath, rather than to receiver-side crustal structure, allowing investigation of mantle heterogeneities without contamination from Moho-induced biases.

4.2 Discussion of uncertainties

The beamforming procedure described in Section 3.1 involves several methodological choices, each of which can influence the analysis presented here. For instance, the chosen frequency band can introduce non-uniqueness in the estimated slowness and backazimuth (i.e., spatial aliasing), depending on the array aperture and station spacing. Some studies advocate for event-specific frequency tuning to optimize signal coherence and resolution (e.g., Schumacher et al., 2018; Rochira et al., 2022). Furthermore, the frequency band of observed signals and the array aperture are inherently intertwined. As noted by Rost and Thomas (2009), the resolving power of a seismic array depends critically on the relationship between the wavelength of the seismic waves (inversely related to frequency) and the aperture of the array. For optimal slowness and backazimuth resolution, the array aperture should be comparable to or larger than the dominant wavelength. To explore this dependency, we experimented with different array sizes (100 km, 250 km, and 500 km) and fixed the upper frequency cutoff at 0.5 Hz (e.g., Rost and Thomas, 2002, 2009) while experimenting with three alternative lower frequency cutoffs (0.075 Hz, 0.1 Hz, and 0.15 Hz). We chose to use the bandpass of 0.05–0.5 Hz as it resulted in the least amount of aliasing and clearest arrivals across events. We also found that in Alaska, where station density is relatively low, specifying a smaller aperture often resulted in selecting fewer stations per sub-array, which in turn produced vespagrams with lower quality and increased aliasing. Although theoretically larger apertures are more susceptible to aliasing, in our case, the increased number of available stations helped mitigate this issue and often led to well-constrained vespagrams. Therefore, the aperture and frequency values used in this study were selected through trial and error to balance aliasing, station availability, and vespagram quality in Alaska. These choices affect the resolution and robustness of individual slowness and backazimuth measurements, and may influence the exact magnitude of measured offsets, but they do not alter the main conclusion that systematic backazimuth deviations in Alaska are consistent with Moho structure and are substantially larger than those observed in the flat-Moho control region.

The dependence of observed backazimuth offsets on underlying structure, particularly Moho gradients, is closely related to the aperture of the sub-arrays. Since each sub-array has a specific aperture, it samples the Moho gradient across a specific area. Additionally, the Fresnel zones of waves impose a spatial averaging effect on the sampled structure. For P-waves at Moho depths, the Fresnel zone radius corresponding to the frequency of 0.157 Hz (the dominant frequency of our selected band) is approximately 25 km, as estimated using Equation 1 of Gudmundsson (1996). However, because each station has its own Fresnel zone, the array effectively samples a region comparable to its surface aperture plus approximately one Fresnel-zone radius on either side, which remains small relative to the ~275 km radius used to compute the local Moho gradient and

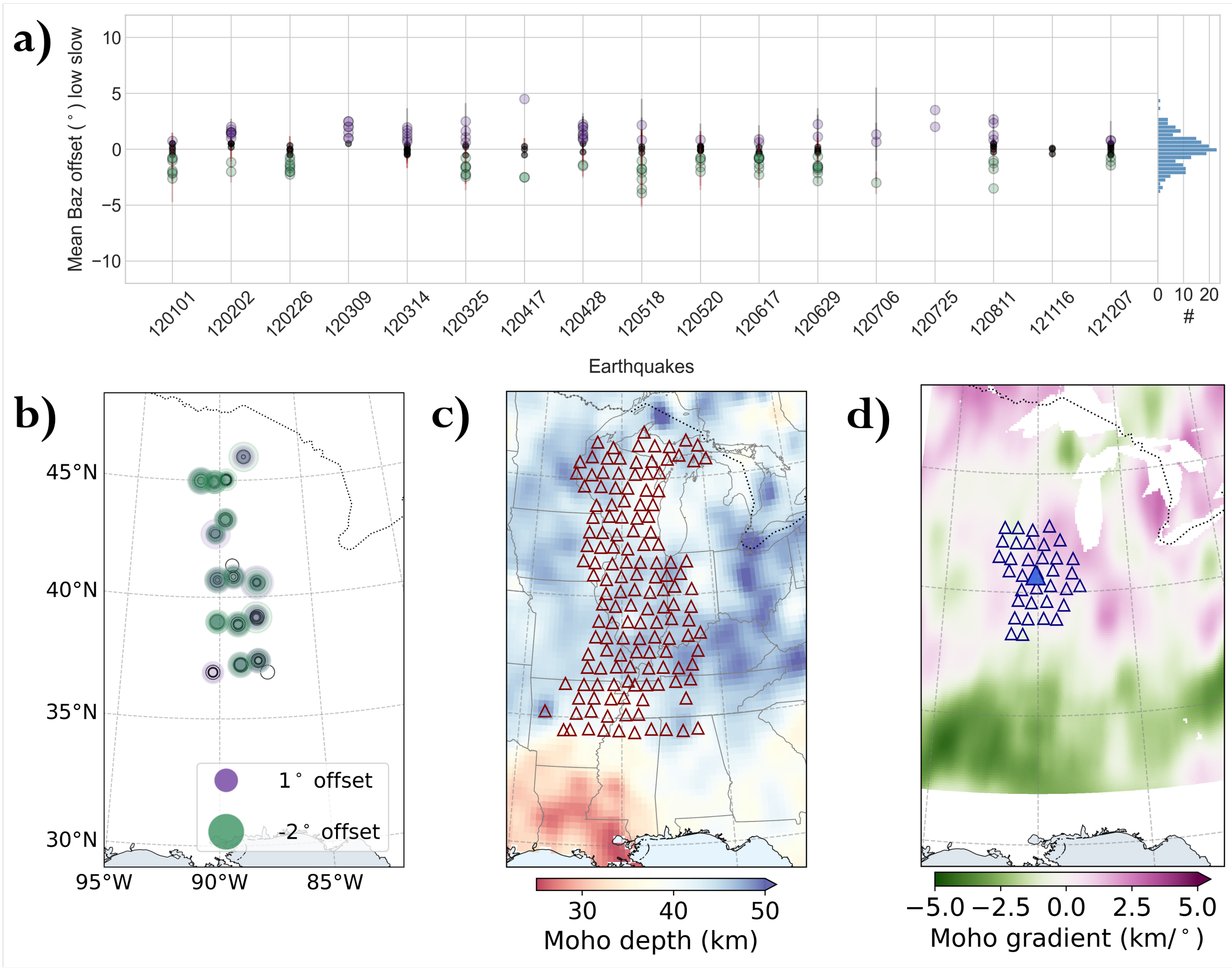

Figure 7 Same as Fig. 5, but for the control case analysis in Section 3.6, using Transportable Array seismic stations (red triangles in c). Moho surface in c) is from Shen and Ritzwoller (2016) and McCafferty et al. (2023).

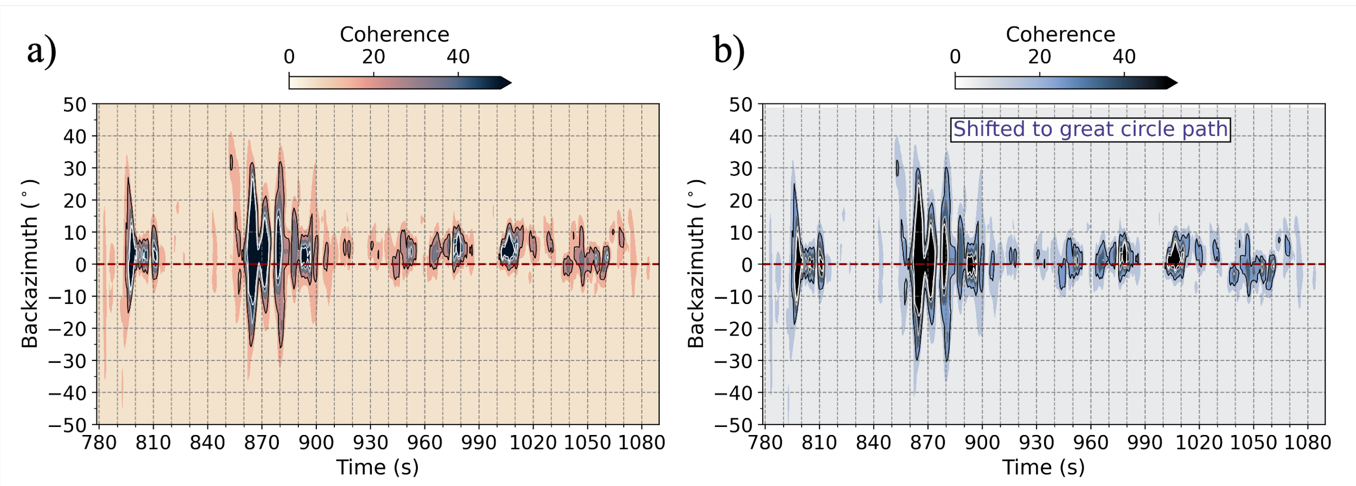

Figure 8 (a) An example vespagram in backazimuth–time space showing significant backazimuth offsets, evident from the dark coherence lobes being shifted away from the great-circle path (red dashed line). (b) The same vespagram as in (left), corrected for Moho structure. The best-fitting Moho tilt that realigns the lobes with the great-circle path was found to be 2.7°.

therefore does not significantly influence our gradient estimates. Despite this, the large aperture of our subarrays mean that the Moho structure is averaged over a similarly broad area. As a result, smaller-scale heterogeneity in Moho topography may be smoothed and may contribute less to the observed backazimuth offsets.

Further, it is important to note that our ray-theory based synthetic tests in Section 2 do not include finitefrequency wavefield effects. As a result, they should be regarded as the upper limit estimate of the effect of Moho topography. Wavelength-dependent spatial averaging may reduce sensitivity to small-scale Moho heterogeneity relative to the ray-theoretical prediction and could result in smaller values than predicted by ray-theory.

4.3 Other possible origins of backazimuth-offsets

Backazimuth offsets observed in array studies are often attributed to structural complexities in the crust or lithosphere directly beneath the array (e.g., Berteussen, 1976). Previous investigations, particularly those using IMS arrays, have documented systematic backazimuth and slowness biases and occasionally ascribed them to instrumental effects (e.g., Bondár et al., 1999). Here, we find no consistency across a range of sub-arrays and events. Given the similarity of the equipment used for these deployments and that each sub-array contains 14 to 70 stations, it seems improbable that instrumental bias is a dominant source of the offsets observed across arrays.

Surface topographic variation has also been proposed as a source of backazimuth and slowness anomalies. Jacobeit et al. (2013), for example, identified such effects in Kyrgyzstan due to elevation differences among stations. Since station elevation also varies across Alaska (Fig. 3), we accounted for this in our beamforming analysis by incorporating elevation corrections using a typical upper crustal P-wave velocity of 3 km/s. The maximum topographic variation within an individual sub-array is approximately 2500 m. For this array, the maximum moveout associated with topography can be up to 0.8 sec (average being 0.5 sec for all sub-arrays), which is similar in magnitude to the effect of a 5° Moho tilt (moveout up to 1.5 sec). For an event that formed 27 sub-arrays, the average maximum topographic difference is 1550 m with a standard deviation of 600 m, indicating that most sub-arrays are significantly affected by elevation contrasts. Therefore, these effects are explicitly corrected for in our beamforming analysis, ensuring that the residual backazimuth offsets discussed here are not driven by surface topography.

Another possible contributor to backazimuth offsets is the presence of sedimentary cover. A strong velocity contrast between low-velocity sediments and the underlying crust can refract incoming teleseismic wavefronts, as demonstrated for the Gräfenberg array (Krüger and Weber, 1992), where a gently dipping sedimentary layer produced systematic slowness and azimuth anomalies. In Alaska, however, sediment thickness exceeding 300 m is largely restricted to latitudes north of $\sim$67° N (Laske, 1997). Most of our sub-arrays lie south of this region, so sediment-related refraction is unlikely to influence the majority of our measurements. Nonetheless, for the few arrays located farther north, sediments may contribute to the observed offsets and cannot be fully ruled out as a source.

Lateral velocity variations within the crust represent an additional potential source of backazimuth and slowness anomalies. In the synthetic tests, we assume a laterally uniform crustal velocity, but real crustal structure across Alaska includes significant velocity heterogeneity. To assess the potential influence of such variations, we performed a synthetic test in which we introduced a $\sim$10% lateral velocity contrast across the crust (V_p = 5.5 km/s vs. 6.0 km/s) while keeping the Moho flat, and applied the same wavefront optimization procedure as in Section 2.2 (Fig. 9a). This configuration produces backazimuth deviations of up to 1.2° and slowness deviations of up to 0.375 s/° (Fig. 9b). Compared to the tilted Moho case (Fig. 2b), the resulting backazimuth deviations are up to 80%, demonstrating that Moho topography is the dominant contributor to the backazimuth offsets we observe. However, the slowness deviations approach up to 70% of the values produced by Moho tilt, suggesting that slowness is more sensitive to lateral crustal velocity variations than backazimuth. Given that our analysis focuses primarily on backazimuth offsets, and that our observed offsets are well reproduced by Moho tilt alone, we do not apply explicit corrections for lateral crustal velocity variations. Nevertheless, we note that in regions where crustal velocity structure is particularly heterogeneous, such effects may contribute to residual slowness anomalies that are not fully accounted for by the Moho correction alone.

Crustal anisotropy is another plausible contributor to the refraction of teleseismic wavefronts (e.g., Bokelmann, 1995b). In Alaska, significant lateral variations in crustal anisotropy have been reported, with differing fast-axis orientations and strength across tectonic provinces (Feng and Ritzwoller, 2019; Berg et al., 2020; Liu and Ritzwoller, 2024). These spatially variable anisotropic effects could influence apparent slowness and backazimuth. However, due to the large aperture of our arrays and the complex and non-uniform nature of the reported anisotropy, we expect that this would likely not significantly affect our observations, and so we do not apply explicit corrections for anisotropy in this analysis.

A further possible source of wavefront refraction is the velocity heterogeneity caused by the subducting Pacific plate along the Alaska-Aleutian subduction zone. Given the location of the slab on the south margin of Alaska, its influence is largely confined to the forearc and central valley regions (Jadamec and Billen, 2010; Rodgers, 2025). Sub-arrays located north of 63° N and east of 150° W likely lie beyond the slab's influence. In addition, raypaths from majority of earthquakes (in the Pacific) typically sample mantle west or southwest of the arrays, further reducing the likelihood of slab-related deflection. For forearc sub-arrays, however, slab contributions cannot be entirely excluded and may help explain the more complex offset patterns observed above the Alaskan forearc (Fig. 5b).

In spite of these other possible causes, our results demonstrate that the majority of the observed backazimuth offsets can be explained by Moho topography, as our synthetic tests show that Moho tilts representative of Alaska (6°) reproduce offsets of 3–5°, consistent with the observations.

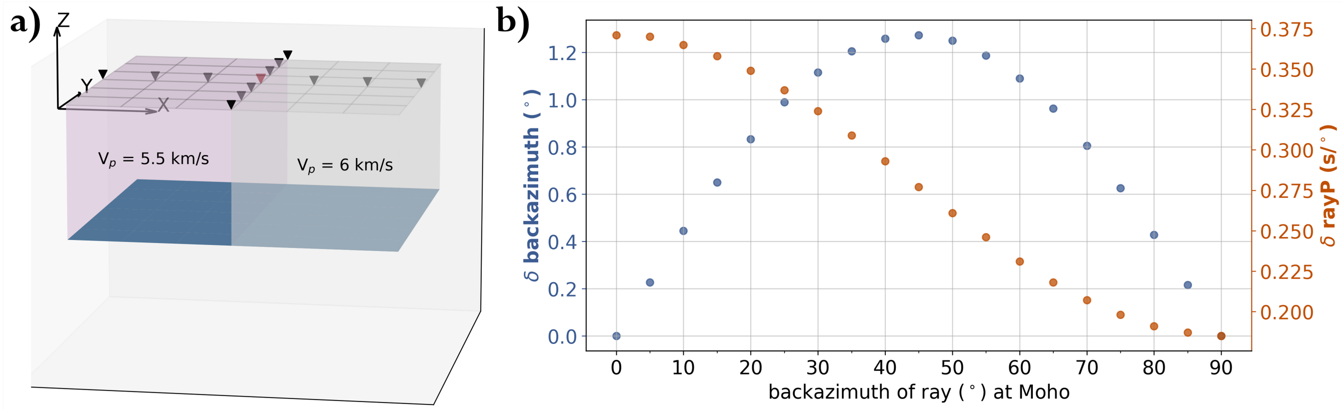

Figure 9 (a) Schematic of the model with a ∼10% lateral crustal velocity variation (V_p = 5.5 km/s and 6.0 km/s) and a flat Moho (blue plane). The overall setup is otherwise identical to Fig. 2a. (b) Same as Fig. 2b, but for the velocity structure shown in (a).

5 Conclusions

We analyzed P-wave energy for 31 teleseismic events recorded by seismic stations in Alaska. By beamforming at sub-arrays of stations across Alaska, we observed systematic shifts in the observed backazimuth of energy of the P and P-depth phases from the great-circle path, with a dependence on sub-array location and source-receiver path. Through synthetic tests, we demonstrate that topography on the Moho, such as exists under Alaska, can account for the observed offsets in backazimuth by refracting incoming wavefronts. Using a plane-wave approximation interacting with a dipping Moho interface, we replicate backazimuth offset values consistent with those observed in array data from Alaska. These findings highlight a critical consideration for seismic imaging: backazimuth deviations introduced by near-surface structure can lead to systematic errors in the measured incoming direction, and consequently, the inferred location of mantle scatterers. Although Moho topography explains the majority of the backazimuth offsets, other factors, including lateral crustal velocity structure, array geometry, crustal anisotropy, sediments, and slab-related heterogeneity, may also contribute. The associated slowness perturbations are small in our observations, however, synthetic tests suggest that we cannot rule out the possibility of slowness anomalies from similar Moho-induced effects. Therefore, incorporating crustal corrections into beamforming analyses is essential for improving the accuracy of deep Earth imaging.

Acknowledgements

We thank two anonymous reviewers for their constructive comments and the editor, György Hetényi, for handling the manuscript. We acknowledge the developers of ObsPy (Krischer et al., 2015), Generic Mapping Tools (Wessel et al., 2019), Scientific Colour Maps (Crameri, 2018), PyGMT (Uieda et al., 2021), and TauP (Crotwell et al., 1999).

Data and code availability

The beamforming code and scripts to generate the figure can be found on Zenodo (Agrawal et al., 2026, https://github.com/wa-v-es/Alaska_baz_offsets). All the raw seismic waveforms used in this study are available via IRIS (http://service.iris.edu/fdsnws/dataselect/1). The networks used are: AK (Alaska Earthquake Center, Univ. of Alaska Fairbanks, 1987), AT (NOAA National Oceanic and Atmospheric Administration (USA), 1967), AV (Alaska Volcano Observatory/USGS, 1988), and CN (Natural Resources Canada, 1975). All figures have been built using Matplotlib (Hunter, 2007), GMT (Wessel et al., 2019), and Cartopy (Met Office, 2010 - 2015).

Competing interests

The authors have no competing interests.

References

Agrawal, S., Frost, D. A., and Crotwell, P. Beamforming and analysis code for "Influence of Moho topography on seismic beamforming: implications for mantle scattering", 2026. doi: 10.5281/ZENODO.19053135.

Alaska Earthquake Center, Univ. of Alaska Fairbanks. Alaska Geophysical Network, 1987. doi: 10.7914/SN/AK.

Alaska Volcano Observatory/USGS. Alaska Volcano Observatory, 1988. doi: 10.7914/SN/AV.

Bagley, B., Courtier, A. M., and Revenaugh, J. Seismic shear wave reflectivity structure of the mantle beneath northeast China and the northwest Pacific. *Journal of Geophysical Research: Solid Earth*, 118(10):5417–5427, Oct. 2013. doi: 10.1002/jgrb.50385.

Bentham, H. L. M. and Rost, S. Scattering beneath Western Pacific subduction zones: evidence for oceanic crust in the mid-mantle. *Geophysical Journal International*, 197(3):1627–1641, Apr. 2014. doi: 10.1093/gji/ggu043.

Berg, E. M., Lin, F., Allam, A., Schulte-Pelkum, V., Ward, K. M., and Shen, W. Shear Velocity Model of Alaska Via Joint Inversion of Rayleigh Wave Ellipticity, Phase Velocities, and Receiver Functions Across the Alaska Transportable Array. *Journal of Geophysical Research: Solid Earth*, 125(2), Feb. 2020. doi: 10.1029/2019jb018582.

Berteussen, K. The origin of slowness and azimuth anomalies at large arrays. *Bulletin of the Seismological Society of America*, 66 (3):719–741, 1976.

Bokelmann, G. H. Azimuth and slowness deviations from the GERESS regional array. *Bulletin of the Seismological Society of America*, 85(5):1456–1463, 1995a. doi: 10.1785/BSSA0850051456.

Bokelmann, G. H. R. P-wave array polarization analysis and effective anisotropy of the brittle crust. *Geophysical Journal International*, 120(1):145–162, Jan. 1995b. doi: 10.1111/j.1365-246x.1995.tb05917.x.

Bondár, I., North, R. G., and Beall, G. Teleseismic slowness-azimuth station corrections for the International Monitoring System Seismic Network. *Bulletin of the Seismological Society of America*, 89(4):989–1003, Aug. 1999. doi: 10.1785/bssa0890040989.

Chen, M., Tromp, J., Helmberger, D., and Kanamori, H. Waveform modeling of the slab beneath Japan. *Journal of Geophysical Research: Solid Earth*, 112(B2), Feb. 2007. doi: 10.1029/2006jb004394.

Colavitti, L., Hetényi, G., and Group, A. W. A new approach to construct 3-D crustal shear-wave velocity models: method description and application to the Central Alps. *Acta Geodaetica et Geophysica*, 57(4):529–562, Nov. 2022. doi: 10.1007/s40328-022-00394-4.

Cormier, V. F. Slab diffraction of S waves. *Journal of Geophysical Research: Solid Earth*, 94(B3):3006–3024, Mar. 1989. doi: 10.1029/jb094ib03p03006.

Crameri, F. Scientific colour maps. *Zenodo*, 10:5281, 2018. doi: 10.5281/zenodo.1243862.

Crotwell, H. P., Owens, T. J., and Ritsema, J. The TauP Toolkit: Flexible Seismic Travel-time and Ray-path Utilities. *Seismological Research Letters*, 70(2):154–160, Mar. 1999. doi: 10.1785/gssrl.70.2.154.

Davies, D., Kelly, E. J., and Filson, J. R. Vespa Process for Analysis of Seismic Signals. *Nature Physical Science*, 232(27), 1971. doi: 10.1038/physci232008a0.

Faber, S., Plomerová, J., Babuška, V., et al. Deep-seated lateral velocity variations beneath the GRF array inferred from mislocation patterns and P residuals. *Journal of Geophysics*, 60(1): 139–148, 1986.

Feng, L. and Ritzwoller, M. H. A 3-D shear velocity model of the crust and uppermost mantle beneath Alaska including apparent radial anisotropy. *Journal of Geophysical Research: Solid Earth*, 124(10):10468–10497, 2019. doi: 10.1029/2019JB018122.

Flanagan, M. P., Myers, S. C., and Simmons, N. A. Model-based corrections to observed back azimuth and slowness observations from a dipping Mohorovicic discontinuity. Technical report, Lawrence Livermore National Laboratory (LLNL), Livermore, CA, 2012.

Frost, D., Garnero, E., Creasy, N., Wolf, J., Bozdag, E., Long, M., Aderoju, A., and Vite, R. Heterogeneous mantle effects on the behaviour of SmKS waves and outermost core imaging. *Geophysical Journal International*, 237(3):1655–1673, 2024. doi: 10.2172/2377938.

Frost, D. A. and Rost, S. The P-wave boundary of the Large-Low Shear Velocity Province beneath the Pacific. *Earth and Planetary Science Letters*, 403:380–392, Oct. 2014. doi: 10.1016/j.epsl.2014.06.046.

Frost, D. A., Rost, S., Selby, N. D., and Stuart, G. W. Detection of a tall ridge at the core–mantle boundary from scattered PKP energy. *Geophysical Journal International*, 195(1), 2013. doi: 10.1093/gji/ggt242.

Frost, D. A., Rost, S., Garnero, E. J., and Li, M. Seismic evidence for Earth's crusty deep mantle. *Earth and Planetary Science Letters*, 470, 2017. doi: 10.1016/j.epsl.2017.04.036.

Frost, D. A., Garnero, E. J., and Rost, S. Dynamical links between small-and large-scale mantle heterogeneity: Seismological evidence. *Earth and Planetary Science Letters*, 482:135–146, Jan. 2018. doi: 10.1016/j.epsl.2017.10.058.

Frost, D. A., Romanowicz, B., and Roecker, S. Upper mantle slab under Alaska: contribution to anomalous core-phase observations on south-Sandwich to Alaska paths. *Physics of the Earth and Planetary Interiors*, 299:106427, Feb. 2020. doi: 10.1016/j.pepi.2020.106427.

Gu, Y. J., An, Y., Sacchi, M., Schultz, R., and Ritsema, J. Mantle reflectivity structure beneath oceanic hotspots. *Geophysical Journal International*, 178(3), 2009. doi: 10.1111/j.1365-246x.2009.04242.x.

Gudmundsson, O. On the effect of diffraction on traveltime measurements. *Geophysical Journal International*, 124(1):304–314, Jan. 1996. doi: 10.1111/j.1365-246x.1996.tb06372.x.

Hao, C. and Zheng, Z. P-Wave Back-Azimuth and Slowness Anomalies Observed by an IMS Seismic Array LZDM. *Bulletin of the Seismological Society of America*, 100(2):657–669, Mar. 2010. doi: 10.1785/0120090059.

Havskov, J. and Kanasewich, E. R. Determination of the dip and strike of the Moho from array analysis. *Bulletin of the Seismological Society of America*, 68(5):1415–1419, Oct. 1978. doi: 10.1785/bssa0680051415.

Hetényi, G., Molinari, I., Clinton, J., Bokelmann, G., Bondár, I., Crawford, W. C., Dessa, J.-X., Doubre, C., Friederich, W., Fuchs, F., et al. The AlpArray Seismic Network: A Large-Scale European Experiment to Image the Alpine Orogen. *Surveys in Geophysics*, 39(5):1009–1033, Apr. 2018. doi: 10.1007/s10712-018-9472-4.

Hunter, J. D. Matplotlib: A 2D Graphics Environment. *Computing in Science & Engineering*, 9(3):90–95, 2007. doi: 10.1109/mcse.2007.55.

IRIS Transportable Array. USArray Transportable Array, 2003. doi: 10.7914/SN/TA.

Jacobeit, E., Thomas, C., and Vernon, F. Influence of station topography and Moho depth on the mislocation vectors for the Kyrgyz Broadband Seismic Network (KNET). *Geophysical Journal International*, 193(2):949–959, Feb. 2013. doi: 10.1093/gji/ggt014.

Jadamec, M. A. and Billen, M. I. Reconciling surface plate motions with rapid three-dimensional mantle flow around a slab edge. *Nature*, 465(7296):338–341, May 2010. doi: 10.1038/nature09053.

Kaneshima, S. Seismic scatterers in the mid-lower mantle. *Physics of the Earth and Planetary Interiors*, 257:105–114, Aug. 2016. doi: 10.1016/j.pepi.2016.05.004.

Kaneshima, S. and Helffrich, G. Small scale heterogeneity in the mid-lower mantle beneath the circum-Pacific area. *Physics of the Earth and Planetary Interiors*, 183(1-2):91–103, Nov. 2010. doi: 10.1016/j.pepi.2010.03.011.

Kennett, B. L. N. and Engdahl, E. R. Traveltimes for global earthquake location and phase identification. *Geophysical Journal International*, 105(2):429–465, May 1991. doi: 10.1111/j.1365-246x.1991.tb06724.x.

Koch, K. and Kradolfer, U. Investigation of azimuth residuals observed at stations of the GSETT-3 Alpha network. *Bulletin of the Seismological Society of America*, 87(6):1576–1597, Dec. 1997. doi: 10.1785/bssa0870061576.

Koch, K. and Kradolfer, U. Determination of Mislocation Vectors to Evaluate bias at GSETT-3 primary stations. *Journal of Seismology*, 3(2):139–151, Apr. 1999. doi: 10.1023/a:1009823825899.

Krischer, L., Megies, T., Barsch, R., Beyreuther, M., Lecocq, T., Caudron, C., and Wassermann, J. ObsPy: a bridge for seismology into the scientific Python ecosystem. *Computational Science & Discovery*, 8(1):014003, May 2015. doi: 10.1088/1749-4699/8/1/014003.

Krüger, F. and Weber, M. The effect of low-velocity sediments on the mislocation vectors of the GRF array. *Geophysical Journal International*, 108(1):387–393, Jan. 1992. doi: 10.1111/j.1365-246x.1992.tb00866.x.

Laske, G. A global digital map of sediment thickness. *Eos Trans. AGU*, 78:F483, 1997.

Li, J., Tian, D., Sun, D., and Tong, P. D" structures beneath the East China Sea resolved by P-wave slowness anomalies. *Journal of Geophysical Research: Solid Earth*, 129(11), Nov. 2024. doi: 10.1029/2024jb029584.

Lindquist, K. G., Tibuleac, I. M., and Hansen, R. A. A Semiautomatic Calibration Method Applied to a Small-Aperture Alaskan Seismic Array. *Bulletin of the Seismological Society of America*, 97 (1B):100–113, Feb. 2007. doi: 10.1785/0120040119.

Liu, C. and Ritzwoller, M. H. Seismic Anisotropy and Deep Crustal Deformation Across Alaska. *Journal of Geophysical Research: Solid Earth*, 129(5), Apr. 2024. doi: 10.1029/2023jb028525.

Martin, C., Bodin, T., and Cottaar, S. Mapping structures on the core–mantle boundary using Sdiff postcursors: Part I. Method and Validation. *Geophysical Journal International*, 235(3), 2023. doi: 10.1093/gji/ggad340.

McCafferty, A., San Juan, C., Lawley, C., Graham, G., Gadd, M., Huston, D., Kelley, K., Paradis, S., Peter, J., and Czarnota, K. National-scale geophysical, geologic, and mineral resource data and grids for the United States, Canada, and Australia: Data in support of the tri-national critical minerals mapping initiative: US Geological Survey, Data release, 2023.

Met Office. *Cartopy: a cartographic python library with a Matplotlib interface*. Exeter, Devon, 2010 - 2015. https://scitools.org.uk/cartopy.

Miller, M. S. and Moresi, L. Mapping the Alaskan Moho. *Seismological Research Letters*, 89(6):2430–2436, Oct. 2018. doi: 10.1785/0220180222.

Murdie, R. E., Yuan, H., O'Donnell, J. P., Johnson, S. P., Ebrahimi, R., and Rashidifard, M. WA Array: A High-Resolution Passive-Source Seismic Survey to Image the West Australian Lithosphere. *Seismological Research Letters*, 95(5), 2024. doi: 10.1785/0220230415.

Natural Resources Canada. Canadian National Seismograph Network. *International Federation of Digital Seismograph Networks*, 1975. doi: 10.7914/SN/CN.

Niazi, M. Corrections to apparent azimuths and travel-time gradients for a dipping Mohorovičić discontinuity. *Bulletin of the Seismological Society of America*, 56(2):491–509, Apr. 1966. doi: 10.1785/bssa0560020491.

NOAA National Oceanic and Atmospheric Administration (USA). National Tsunami Warning Center Alaska Seismic Network, 1967. doi: 10.7914/SN/AT.

Pirli, M., Pirlis, E., and Voulgaris, N. Mislocation vectors for the Tripoli seismic array, Greece, and structural effect implications from backazimuth and slowness residual analysis. *Bulletin of the Geological Society of Greece*, 40(3), 2018. doi: 10.12681/bgsg.16876.

Pisconti, A., Rochira, F., and Thomas, C. Out-of-plane signals from deep mantle subducted slabs at teleseismic distances: insights from three-dimensional global modelling and three-component array analysis. *Geophysical Journal International*, 242(3), 2025. doi: 10.1093/gji/ggaf248.

Ram, A. and Yadav, L. Structural corrections for slowness and azimuth of seismic signals arriving at Gauribidanur array. *Bulletin of the Seismological Society of America*, 74(1):97–105, Feb. 1984. doi: 10.1785/bssa0740010097.

Rochira, F., Schumacher, L., and Thomas, C. Mapping the edge of subducted slabs in the lower mantle beneath southern Asia. *Geophysical Journal International*, 230(2):1239–1252, Mar. 2022. doi: 10.1093/gji/ggac110.

Rodgers, A. AK112: Full Waveform Inversion Tomography of Alaska Improves Waveform Fits While Imaging Crustal, Mantle, and Slab Structure. *The Seismic Record*, 5(3):270–280, 2025. doi: 10.1785/0320250003.

Rost, S. and Thomas, C. Array seismology: methods and applications. *Reviews of Geophysics*, 40(3), 2002. doi: 10.1029/2000rg000100.

Rost, S. and Thomas, C. *Improving Seismic Resolution Through Array Processing Techniques*, page 3–31. Springer Netherlands, 2009. doi: 10.1007/978-90-481-3680-3_2.

Rost, S., Garnero, E. J., and Williams, Q. Seismic array detection of subducted oceanic crust in the lower mantle. *Journal of Geophysical Research: Solid Earth*, 113(B6), 2008. doi: 10.1029/2007jb005263.

Rost, S., Frost, D. A., Nowacki, A., and Cobden, L. Wavefield distortion imaging of Earth's deep mantle. *Earth and Planetary Science Letters*, 604:118011, Feb. 2023. doi: 10.1016/j.epsl.2023.118011.

Schumacher, L. and Thomas, C. Detecting lower-mantle slabs beneath Asia and the Aleutians. *Geophysical Journal International*, 205(3):1512–1524, Mar. 2016. doi: 10.1093/gji/ggw098.

Schumacher, L., Thomas, C., and Abreu, R. Out-of-plane seismic reflections beneath the Pacific and their geophysical implications. *Journal of Geophysical Research: Solid Earth*, 123(3):2286–2302, Mar. 2018. doi: 10.1002/2017jb014728.

Schweitzer, J., Fyen, J., Mykkeltveit, S., Gibbons, S. J., Pirli, M., Kühn, D., and Kværna, T. Seismic arrays. In *New manual of seismological observatory practice 2 (NMSOP-2)*, pages 1–80. Deutsches GeoForschungsZentrum GFZ, 2012.

Selby, N. D. Application of a Generalized F Detector at a Seismometer Array. *Bulletin of the Seismological Society of America*, 98(5): 2469–2481, Oct. 2008. doi: 10.1785/0120070282.

Shen, W. and Ritzwoller, M. H. Crustal and uppermost mantle structure beneath the United States. *Journal of Geophysical Research: Solid Earth*, 121(6), 2016. doi: 10.1002/2016jb012887.

Silver, P. G. and Chan, W. W. Observations of body wave multipathing from broadband seismograms: Evidence for lower mantle slab penetration beneath the Sea of Okhotsk. *Journal of Geophysical Research: Solid Earth*, 91(B14):13787–13802, Dec. 1986. doi: 10.1029/jb091ib14p13787.

Stockmann, F., Cobden, L., Deschamps, F., Fichtner, A., and Thomas, C. Investigating the seismic structure and visibility of dynamic plume models with seismic array methods. *Geophysical Journal International*, 219(Supplement_1):S167–S194, Aug. 2019. doi: 10.1093/gji/ggz334.

Tibuleac, I. M. and Stroujkova, A. Calibrating the Chiang Mai seismic array (CMAR) for improved event location. *Seismological Research Letters*, 80(4):579–590, 2009. doi: 10.1785/gssrl.80.4.579.

Uieda, L., Tian, D., Leong, W. J., Toney, L., Schlitzer, W., Grund, M., Newton, D., Ziebarth, M., Jones, M., and Wessel, P. PyGMT: A Python interface for the generic mapping tools. *Zenodo*, 2021. doi: 10.5281/zenodo.5607255.

Vidale, J. E. Waveform effects of a high-velocity, subducted slab. *Geophysical Research Letters*, 14(5):542–545, May 1987. doi: 10.1029/gl014i005p00542.

Ward, J., Thorne, M., Nowacki, A., and Rost, S. Automatic Slowness Vector Measurements of Seismic Arrivals with Uncertainty Estimates using Bootstrap Sampling, Array Methods and Unsupervised Learning. *Geophysical Journal International*, 226(3): 1847–1857, 2021. doi: 10.1093/gji/ggab196.

Ward, J., Thorne, M., Nowacki, A., and Rost, S. Upper mantle structure beneath the contiguous US resolved with array observations of SKS multipathing and slowness vector perturbations. *Journal of Geophysical Research: Solid Earth*, 128(7): e2022JB026260, 2023. doi: 10.1029/2022JB026260.

Wessel, P., Luis, J. F., Uieda, L. a., Scharroo, R., Wobbe, F., Smith, W. H., and Tian, D. The generic mapping tools version 6. *Geochemistry, Geophysics, Geosystems*, 20(11):5556–5564, 2019. doi: 10.1029/2019GC008515.

Wolf, J., Frost, D. A., Long, M. D., Garnero, E., Aderoju, A. O., Creasy, N., and Bozdağ, E. Observations of mantle seismic anisotropy using array techniques: Shear-wave splitting of beamformed SmKS phases. *Journal of Geophysical Research: Solid Earth*, 128 (1), Dec. 2022. doi: 10.1029/2022jb025556.

Wolf, J., Long, M. D., and Frost, D. A. Ultralow velocity zone and deep mantle flow beneath the Himalayas linked to subducted slab. *Nature Geoscience*, 17(4):302–308, Feb. 2024. doi: 10.1038/s41561-024-01386-5.

Wright, C., Cleary, J. R., and Muirhead, K. J. The Effects of Local Structure and the Adjacent Upper Mantle on Short-Period P Wave Arrivals Recorded at the Warramunga Seismic Array. *Geophysical Journal International*, 36(2):295–319, Feb. 1974. doi: 10.1111/j.1365-246x.1974.tb03641.x.

Yuan, Y., Sun, D., and Thomas, C. A New Seismic Phase to Detect Mid-Mantle Scatterers. *Geophysical Research Letters*, 50(2), Jan. 2023. doi: 10.1029/2022gl100236.

Zengeni, T. G. A note on an azimuthal correction for dT/dΔ for a single dipping plane interface. *Bulletin of the Seismological Society of America*, 60(2):299–306, Apr. 1970. doi: 10.1785/bssa0600020299.

Zhan, Z., Helmberger, D. V., and Li, D. Imaging subducted slab structure beneath the Sea of Okhotsk with teleseismic waveforms. *Physics of the Earth and Planetary Interiors*, 232, 2014. doi: 10.1016/j.pepi.2014.03.008.